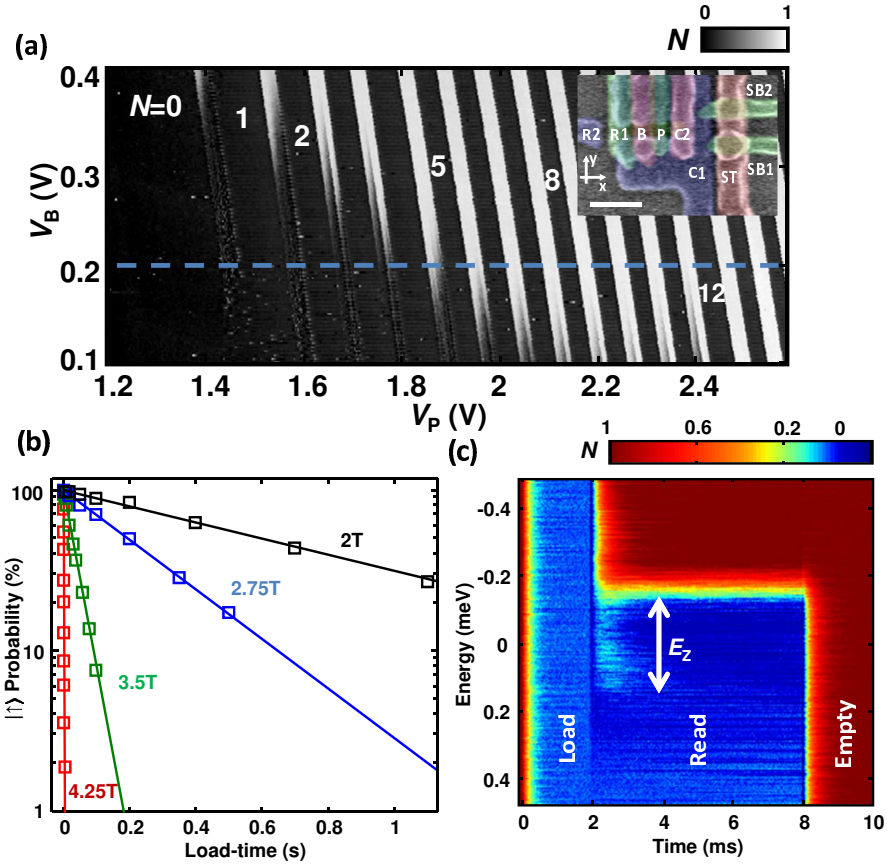

Supplementary Figure S1: Charge and spin detection. (a) Pulsed-voltage charge stability diagram with an applied square pulse of 32 mV peak-to-peak at 287 Hz. Grey-scale indicates the excess electron occupancy in the dot (ΔN) for each charge addition. Inset: False-color scanning electron micrograph of a device identical to the one used for experiments. Color code identifies different layers in the gate stack. Scale bar length is 100 nm. (b) Exponential decays of the spin-up probabilities at different magnetic fields. Solid lines are single-exponential fits of the measured data (squared points) leading to the evaluation of T_1 times. (c) QD occupancy during a 3-level pulse with varying read-phase level. The energy axis shows the dot's electrochemical potential during the read phase. Each trace is averaged over 256 single-shots. Applied field $B = 3$ T. Zeeman splitting can be evaluated from the current transient energy range.

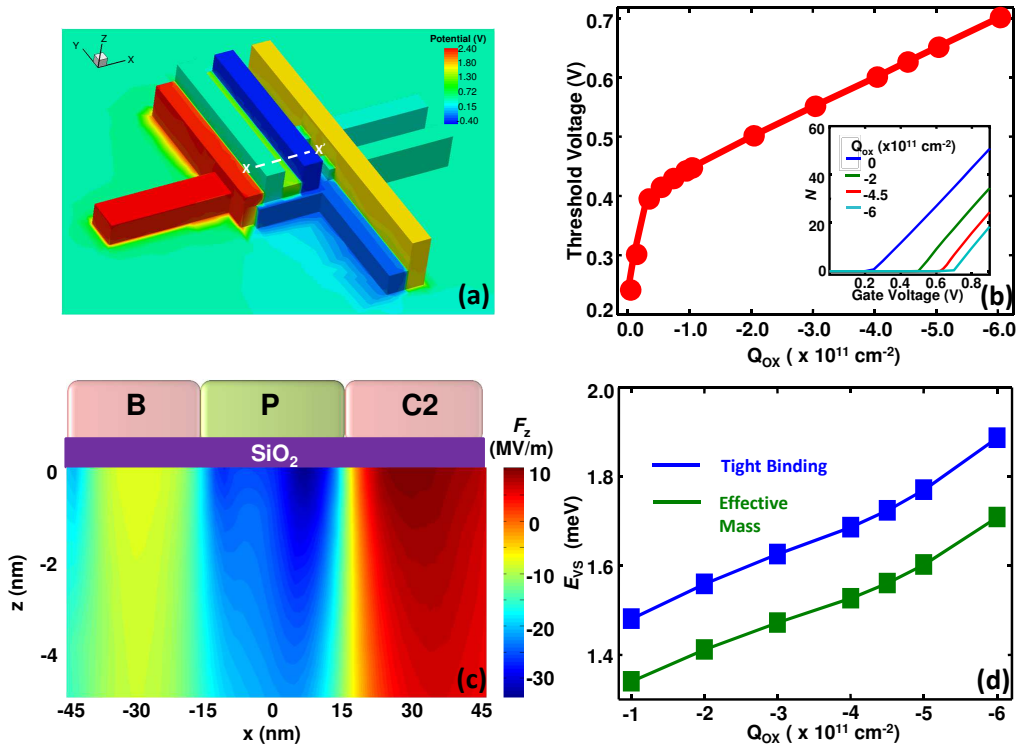

Supplementary Figure S2: TCAD simulations. (a) Three-dimensional device layout used for the simulations. Color scale represents the electrostatic potential at each gate for one iteration. (b) Calculated threshold voltage as a function of interface charge. The experimental value (0.625V) is obtained at $Q_{\rm ox} = -4.5 \times 10^{11}$ cm^{-2}. Inset: integrated electron density in the dot vs the voltage applied simultaneously to all gates for different $Q_{\rm ox}$. Threshold voltage dependence on $Q_{\rm ox}$ can be extracted (main graph). (c) Two-dimensional electric field profile at $V_{\rm P}$=1.4V. (d) Valley splitting at $V_{\rm P}$=1.4V as a function of interface charge calculated with the atomistic (blue) and effective mass (green) predictions.

Supplementary Note 1

The addition spectrum of the QD is characterized via a technique widely used for GaAs-based systems, which employs both charge detection and gate pulsing[30]. A train of square voltage pulses is applied to gate P, in addition to its dc voltage, shifting the energy levels of the dot up and down. This pulse train modulates the SET sensor current with the same frequency of the pulse due to cross-capacitance effects. The resulting current at this frequency is measured with a lock-in amplifier. Full details of the measurement set-up are reported elsewhere[41]. Supplementary Figure S1 (a) shows the measured stability map as a function of plunger gate voltage, $V_{\rm P}$, and barrier gate voltage, $V_{\rm B}$ (see inset). Current peaks in the lock-in signal indicate the occurrence of charge transitions due to tunnelling between the QD and the reservoir. We have converted this signal into an average change of occupancy[41], ΔN, which is shown in the grey-scale plot. For each transition, we can also probe the first orbital excited state whenever a slow decrease in the detection signal is followed by a steep rise[41]. We observe charge additions for the first fourteen electrons in the dot. In order to translate the voltage dependence of these features into a spectroscopy of the dot's charging energy ($E_{\rm C}$), we determine the voltage to energy conversion factor, α, for gate P via temperature dependence measurements and we find $\alpha \approx 0.16$ eV/V. The dashed horizontal line indicates that the addition spectrum shown in the main article has been obtained for $V_{\rm B}$=0.2V.

Supplementary Note 2

Here, we describe the procedure utilized to measure spin lifetimes for varying B. The probability of observing a spin-up electron, P_{up}, decreases when the loading time, t_{load}, is increased. A threshold detection method[24] is used to determine the fraction of shots that contribute to the spin-up count for each t_{load} at different B. Supplementary Figure S1 (b) shows that the probability is well fitted by a single exponential time decay, $P_{up} \propto e^{-t_{load}/T_1}$, from which $T_1(B)$ is evaluated.

By modifying the pulse sequence and recording readout traces for different voltage levels of the read phase, it is possible to extract the single-particle Zeeman splitting[24]. Indeed, by stepping the read voltage from a level where both spin states are lifted above the Fermi energy of the reservoir to a level where both spin states are pushed below the reservoir's energy, the separation between the two spin states can be evaluated. Supplementary Figure S1 (c) shows the QD occupancy averaged over 256 single-shot traces for varying read levels at B=3T (note that the energy scale on the y-axis is the effective shift of the dot's potential). As explained in the main article, the detection of a spin-up electron would be signalled by a transient in the detector's current. This transient is seen to extend for about 350μeV, as expected from the Zeeman equation, $E_{\rm Z} = g\mu_{\rm B}B$, by assuming $g = 2$. The field dependence of the measured $E_{\rm Z}(B)$ also shows good agreement with the Zeeman equation. This proves that we can reliably load/unload electrons onto spin-split single-particle states.

Supplementary Note 3

We consider a small quantum dot (QD) defined electrostatically in a MOS Si/SiO_2 heterostructure, as described in the main text. For a QD occupied by a single electron the first excited orbital state is some 8 meV above the ground state and it only weakly influences the ground state shell (see however below). Due to strong electric field at the heterostructure, the 6-fold degeneracy of the conduction band electrons is lifted: only two lowest energy valleys remain relevant, at momentums $\boldsymbol{k} \approx k_0\,[\hat{z}, -\hat{z}]$, with $k_0 \simeq 0.85\,\frac{2\pi}{a_0}$; the remaining two-fold degeneracy is lifted via the sharp interface potential, leading to a valley splitting, $E_{\rm VS}$, of the order of few hundred μeV, and linearly proportional to the electric field at the interface, $E_{\rm VS} \simeq \alpha_E \langle E_{\rm interface}\rangle$. This forms the ground state shell of the two lowest valley states, v_1 and v_2; (these approach states of definite parity, $v_{1,2} \to v_{-,+}$ in strong field, as per notation in the main article).

In the effective mass approximation the valley wave functions are generally written as

$$|v_1\rangle = \sum_{i=\pm z} \Phi^i_{v1}(\boldsymbol{r}) \alpha_i^{v_1} u_i(\boldsymbol{r})\, e^{ik_i z} \tag{S1}$$

$$|v_2\rangle = \sum_{i=\pm z} \Phi^i_{v2}(\boldsymbol{r}) \alpha_i^{v_2} u_i(\boldsymbol{r})\, e^{ik_i z}, \tag{S2}$$

where $\psi_i(\boldsymbol{r}) \equiv u_i(\boldsymbol{r})\, e^{ik_i z}$ are the Kohn-Luttinger valley functions, with the periodic part $u_i(\boldsymbol{r})$, and k_i ($i = \pm z$) is the position of the valley minima. Here, $\Phi^i_{v_j}(\boldsymbol{r})$ are the envelope functions corresponding to the orbital ground

state (s-like). In the ideal QD (ideal interface, symmetric circular dot, etc.) the envelopes are separable, e.g.: $\Phi_0^{+z}(\boldsymbol{r}) = F_0(x,y)\, f_0(z)$; generally, the index of the state, v_1 or v_2, distinguishes different envelopes, originating from valley-orbit coupling in the presence of a non-ideal interface, also separability may be lost. The relations: $\Phi_{v_j}^{+z} = \Phi_{v_j}^{-z}$ and $|\alpha_{+z}^{v_j}| = |\alpha_{-z}^{v_j}|$ are maintained for each state by time reversal. For the states of definite parity above, the valley populations are: $\alpha_{+z}^{-} = -\alpha_{-z}^{-} = \frac{1}{\sqrt{2}}$, $\alpha_{+z}^{+} = \alpha_{-z}^{+} = \frac{1}{\sqrt{2}}$.

By switching on a magnetic field, the states are Zeeman split and one gets four lowest spin-valley states denoted as $|1\rangle = |v_1{\downarrow}\rangle$, $|2\rangle = |v_1{\uparrow}\rangle$, $|3\rangle = |v_2{\downarrow}\rangle$, $|4\rangle = |v_2{\uparrow}\rangle$. The corresponding (unperturbed) energies are $E_1 = -E_{\rm Z}/2$, $E_2 = +E_{\rm Z}/2$, $E_3 = E_{\rm VS} - E_{\rm Z}/2$, $E_4 = E_{\rm VS} + E_{\rm Z}/2$, where levels 2 and 3 cross at $E_{\rm Z} = E_{\rm VS}$, and $E_{\rm Z} = g_{Si}\mu_B B$ is the Zeeman splitting. Since electron-phonon interaction does not flip spin, phonon relaxation between $|2\rangle$ and $|1\rangle$ is forbidden, while $|3\rangle$ to $|1\rangle$ is allowed as a pure valley (non-spin flip) relaxation. It is the mixing between valley states $|2\rangle$ and $|3\rangle$ due to spin-orbit coupling (SOC) that causes a renormalized state $|\bar{2}\rangle$ to have a spin-down component, that allows phonon transition $|\bar{2}\rangle \to |1\rangle$ to take place. The SOC interaction forms an anticrossing point for the states $|\bar{2}\rangle$, $|\bar{3}\rangle$, with a splitting Δ_a, where the spin flip is maximal and so is the $|\bar{2}\rangle \to |1\rangle$ relaxation, reaching the order of pure phonon-valley relaxation, which is observed as a relaxation "hot-spot" (see Fig. 2 (c,d) of main text).

Both the anticipated non-zero splitting at the anticrossing of the two valley states, and the phonon relaxation mechanism requires non-zero valley dipole matrix elements: $\boldsymbol{r}_{12} \equiv \langle v_1|\boldsymbol{r}|v_2\rangle$, $\boldsymbol{r}_{11} \equiv \langle v_1|\boldsymbol{r}|v_1\rangle$, and $\boldsymbol{r}_{22} \equiv \langle v_2|\boldsymbol{r}|v_2\rangle$. In the ideal case, however, they will take a non-zero value only from Umklapp (intervalley) contributions, which are highly suppressed in a QD. While a complete theory of the valley wave functions in the presence of a roughness/steps is still under development, some gross effects of the experiment can be explained just by *postulating* non-zero dipole matrix elements. The intravalley contribution is generally given by (it is zero in the ideal case):

$$\begin{aligned}\boldsymbol{r}_{12} &= \langle v_1|\boldsymbol{r}|v_2\rangle \\ &\simeq \sum_{i=\pm z} \alpha_i^{v_1 *}\alpha_i^{v_2} \int d\boldsymbol{r}\, \boldsymbol{r}\, \Phi_{v1}^{i*}(\boldsymbol{r})\Phi_{v2}^{i*}(\boldsymbol{r})\, u_i^*(\boldsymbol{r})u_i(\boldsymbol{r}),\end{aligned} \tag{S3}$$

and similarly for $\boldsymbol{r}_{11}$, $\boldsymbol{r}_{22}$. Numerical fit to the experimental data presented in this paper consistently reveal values of $|\boldsymbol{r}_{12}|$ the order of few nm (these may depend on the applied electric field at the interface, and also on the QD occupancy).

To calculate the splitting at anticrossing of the spin-valley states, $|2\rangle = |v_1{\uparrow}\rangle$, and $|3\rangle = |v_2{\downarrow}\rangle$, we use the spin-orbit coupling (SOC). In two dimensions the well known SOC Hamiltonian reads: $H_{\rm SO} = H_{\rm D} + H_{\rm R}$, with the Dresselhaus and Rashba terms, related to conduction band electrons, confined in a [001] 2DEG:

$$H_D = \beta_D(-\sigma_x P_x + \sigma_y P_y), \quad H_R = \alpha_R(\sigma_x P_y + \sigma_y P_x); \tag{S4}$$

here σ_x, σ_y are the Pauli matrices along the principal crystal axes, and $\boldsymbol{P} = \boldsymbol{p} + e\boldsymbol{A}(\boldsymbol{r})$ is the generalized momentum. Related to current experiment, we consider an in-plane magnetic field, which is parallel to the (110)-direction, and its vector potential in the symmetric gauge reads: $\boldsymbol{A}(\boldsymbol{r}) = \frac{B}{2\sqrt{2}}(z, -z, -x+y)$. Using the eigenoperators $\sigma_{\pm 45} \equiv -(\sigma_x \pm \sigma_y)$, $(\sigma_{+45}|\uparrow,\downarrow\rangle = (\pm)|\uparrow,\downarrow\rangle)$, and Hamiltonian commutation relations one can express the perturbation matrix via dipole matrix elements, e.g.:

$$V_{23} = \langle v_1{\uparrow}\,|H_{SO}|v_2{\downarrow}\rangle = \frac{i\, m_t\, E_{VS}}{\sqrt{2}\hbar}(x_{12} + y_{12})(\beta_D - \alpha_R), \tag{S5}$$

while $V_{12}, V_{13} \approx 0$. Estimation for the splitting gives: $\Delta_a = 2|V_{23}| \approx r \times 0.7\, 10^{-4}\, E_{\rm VS}$, where, we have used transverse mass $m_t \simeq 0.198 m_e$, and $x_{12} = y_{12} \equiv r$ is the dipole size ($z_{12} \approx 0$). We assume a SOC strength $\beta_D - \alpha_R \approx 15\,\mathrm{m/s}$ for an interface field of $10^7\,\mathrm{V/m}$ (implying it may reach $3-4$ higher values in the current experiment). Note, that in general, Δ_a depends linearly on the valley splitting and the dipole matrix element.

To calculate the phonon relaxation rate between the lowest spin-valley states we take into account the hybridization of the levels $|2\rangle$ and $|3\rangle$ due to SOC [see Fig. 2(c)]. The relevant matrix elements

$$\langle\bar{2}|H_{\rm e-ph}|1\rangle = -\cos\frac{\gamma}{2}\,\langle v_2|H_{\rm e-ph}|v_1\rangle \tag{S6}$$

$$\langle\bar{3}|H_{\rm e-ph}|1\rangle = \sin\frac{\gamma}{2}\,\langle v_2|H_{\rm e-ph}|v_1\rangle \tag{S7}$$

$$\langle\bar{3}|H_{\rm e-ph}|\bar{2}\rangle = \frac{1}{2}\sin\gamma\,[\langle v_1|H_{\rm e-ph}|v_1\rangle - \langle v_2|H_{\rm e-ph}|v_2\rangle] \tag{S8}$$

are expressed via the admixture of the state $|3\rangle = |v_2{\downarrow}\rangle$, to the states $|\bar{2}\rangle$, $|\bar{3}\rangle$ (Eqs. (2),(3) of the main text) and via the phonon transition matrix element between the valley states.

Calculation of the valley phonon relaxation rate is performed via the electron-phonon deformation potential interaction[52] in the approximation when only intravalley contributions are taken into account, and using the non-zero dipole matrix element, Eq.(S3). For the relaxation below the anticrossing ($|\bar{2}\rangle \to |1\rangle$) we obtain $\Gamma^{(\sigma)}_{\bar{2}1} = \cos^2\frac{\gamma}{2}\,\Gamma^{(\sigma)}_{v'v}$. Above anticrossing, the experimentally observable transitions are $|\bar{3}\rangle \to |1\rangle$ and $|\bar{3}\rangle \to |\bar{2}\rangle$, see Fig. 2 (c) of main text. (In the second case, a subsequent decay of $|\bar{2}\rangle \to |1\rangle$ above anticrossing is purely valley and therefore very fast). The rates are: $\Gamma^{(\sigma)}_{\bar{3}1} = \sin^2\frac{\gamma}{2}\,\Gamma^{(\sigma)}_{v'v}$ and $\Gamma^{(\sigma)}_{\bar{3}\bar{2}} = \cos^2\frac{\gamma}{2}\,\sin^2\frac{\gamma}{2}\,\Gamma^{(\sigma)}_{v'v}$, respectively. In all three cases above, the valley phonon relaxation rate $\Gamma^{(\sigma)}_{v'v}$ is of the same functional form (we used dipole approximation):

$$\Gamma^{(\sigma)}_{v'v}\left[\Delta E_{v'v}, \boldsymbol{r}_{12}\right] = \frac{1}{4\pi\rho\hbar}\,\frac{\omega^5_{v'v}}{v^7_\sigma}\int_{-1}^{1} dx\, D(x,\boldsymbol{r}_{12})\,\Xi^{(\sigma)}(x) \tag{S9}$$

$$D(x,\boldsymbol{r}_{12}) \equiv \frac{x^2_{12}+y^2_{12}}{2}(1-x^2) + z^2_{12}\,x^2, \quad x \equiv \cos(\theta), \tag{S10}$$

and depends on the actual transition energy $\Delta E_{v'v}$; here $D(x,\boldsymbol{r}_{12})$ depends quadratically on the dipole components $\boldsymbol{r}_{12}$. Note, that for the transition $|\bar{3}\rangle \to |\bar{2}\rangle$ one have to substitute $\boldsymbol{r}_{12}$ by the difference dipole matrix element $\boldsymbol{r}_{11}-\boldsymbol{r}_{22}$. The integrand, that is proportional to the deformation potential constants, Ξ_d, Ξ_u, is: $\Xi^{(l)}(x) = \Xi^2_d + 2\Xi_d\Xi_u x^2 + \Xi^2_u x^4$ for longitudinal phonons, and $\Xi^{(t2)}(x) = \Xi^2_u x^2(1-x^2)$ for transverse phonons.

Using Eq.(S9), one can see that the dependence of the relaxation on magnetic field is $\sim B^5$ far below anticrossing, since the spin admixture coefficient $\cos^2\frac{\gamma}{2} \sim \frac{\Delta^2_a}{4(E_{\rm VS}-E_{\rm Z})^2}$ is only weakly B-dependent for $E_{\rm Z} \ll E_{\rm VS}$. At anticrossing, the mixing between spin-up and spin-down states is maximal, and relaxation reaches a fast (pure valley) transition rate; e.g., for $B = 2.8$T, $\Gamma_{\bar{2}1} \approx 10^7 - 10^8\,s^{-1}$ for $r = 1-3$ nm. Numerical fits to the experimental data show that the intervalley SOC mixing mechanism alone, is not enough to describe the actual B-dependence above anticrossing (except close vicinity of the hot-spot). An additional mechanism of virtual excitation of the first orbital $2p$-state with overall B^7 dependence becomes important at high magnetic fields (see below).

Spin-valley relaxation mechanism in the 2 electron-case.
In considering the two-electron case one replaces the Coulomb interaction by a mean field: $U(\boldsymbol{r}_1,\boldsymbol{r}_2) \approx \tilde{U}(\boldsymbol{r}_1)+\tilde{U}(\boldsymbol{r}_2)$, and the 2-electron wave functions are constructed from the corresponding single-particle states, $\varphi_i(\boldsymbol{r}) \approx |v_i\rangle$, $i = 1,2$, Eqs. (S1),(S2). [The single-particle states in the 2-electron case should include corrections due to the mean field potential, neglected in zeroth-order approximation]. The corresponding spin-valley states are the spin-singlet and spin-triplet:

$$|v'_1, S\rangle = \varphi_1(\boldsymbol{r}_1)\varphi_1(\boldsymbol{r}_2) \otimes \frac{1}{\sqrt{2}}\left[|\uparrow_1\downarrow_2\rangle - |\downarrow_1\uparrow_2\rangle\right] \tag{S11}$$

$$|v'_2, T_-\rangle = \frac{1}{\sqrt{2}}\,\left[\varphi_1(\boldsymbol{r}_1)\varphi_2(\boldsymbol{r}_2) - \varphi_1(\boldsymbol{r}_2)\varphi_2(\boldsymbol{r}_1)\right] \otimes |\downarrow_1\downarrow_2\rangle \qquad . \tag{S12}$$

For the energy difference in the 2-electron case, one have to take account of the Coulomb interaction in the two configurations: $\Delta E_{\rm TS} = E_{\rm T} - E_{\rm S} = E_{\rm VS} + \langle U\rangle_{\rm T} - \langle U\rangle_{\rm S}$. Since the valley states are s-like (and using mean field approximation) one can show that the 2-electron valley splitting coincides with the 1-electron case: $\Delta E_{\rm TS} \simeq E_{\rm VS}$.

Similar to the 1-electron case, one calculates the splitting at anticrossing for the levels $|1\rangle_{2e} = |v'_1, S\rangle$ and $|2\rangle_{2e} = |v'_2, T_-\rangle$. For magnetic field along the (110)-direction the non-diagonal matrix element coincides with the single-particle one, Eq.(S5):

$$V_{12} = \langle 1|H_{SO}|2\rangle = \frac{im_t E_{\rm VS}(\beta_D - \alpha_R)}{\sqrt{2}\hbar}\langle\varphi_1(\boldsymbol{r}_1)|(x_1+y_1)|\varphi_2(\boldsymbol{r}_1)\rangle, \tag{S13}$$

and the splitting is the same as well: $\Delta^{2e}_a = 2|V_{12}| = \Delta_a$. Thus, the hybridized states (in the presence of SOC), are admixtures of $|1\rangle_{2e}$, $|2\rangle_{2e}$, with the same admixture coefficients $\sin\frac{\gamma}{2}$, $\cos\frac{\gamma}{2}$, as for the single-electron case. The electron-phonon matrix element can be calculated: $\langle\bar{2}|H_{\rm e-ph}|\bar{1}\rangle = \frac{1}{2}\sin\gamma\,[\langle v'_1, S|H_{\rm e-ph}|v'_1, S\rangle - \langle v'_2, T_-|H_{\rm e-ph}|v'_2, T_-\rangle]$ and shown to coincide with the 1-electron matrix element of the $\bar{3} \to \bar{2}$ transition: $\langle\bar{2}|H_{\rm e-ph}|\bar{1}\rangle = \langle\bar{3}|H_{\rm e-ph}|\bar{2}\rangle$. Therefore, the corresponding rates also coincide: $\Gamma^{(\sigma)}_{\bar{2}\bar{1}} = \Gamma^{(\sigma)}_{\bar{3}\bar{2}} = \cos^2\frac{\gamma}{2}\,\sin^2\frac{\gamma}{2}\,\Gamma^{(\sigma)}_{v'v}([\Delta E_{v'v}, \boldsymbol{r}_{11}-\boldsymbol{r}_{22}]$, as the energy difference is the same for both transitions. Numerical fit to the data just above anticrossing in the 1-electron case for $E_{\rm VS} = 0.33$ meV, and a fit to the data in the 2-electron case for $E_{\rm VS} = 0.58$ meV (see Fig. 2(d) and Fig. 3(b) of the main text) are consistent with dipole matrix element $\boldsymbol{r}_{11} - \boldsymbol{r}_{22}$ of few nm. Therefore, the experiment inevitably shows that the difference dipole matrix element is non-zero, $\Delta r_{12} \equiv \boldsymbol{r}_{11} - \boldsymbol{r}_{22} \neq 0$.

Including B^7-corrections due to virtual transitions to orbital 2p-states. 1-electron case
In the one electron case we consider orbital excitations above the ground state $|v_1\rangle$, split by $\Delta \simeq 8$ meV. For

an in-plane magnetic field with weak magnetic confinement, we have $\omega_{x,y} \gg \omega_c$ and these states are separable[51]: $|m_1\rangle = |0_x\, 1_y\rangle$, $|m_2\rangle = |1_x\, 0_y\rangle$. The corresponding non-zero dipole matrix elements are $\langle 0|y|m_1\rangle \equiv y_{0m_1} = \langle 0|x|m_2\rangle \equiv x_{0m_2} = \sqrt{\frac{\hbar^2}{2m_t\Delta}}$. SOC makes the qubit states, $|1\rangle$, $|2\rangle$, to mix with these upper orbital states. Calculation in the first order of PT is performed (similarly to Ref.[38]), while we neglect small corrections due to hybridization of the states $|2\rangle$, $|3\rangle$. The resulting rate has the B^7 dependence on the magnetic field (expected for a $1s \to 2p$ virtual transition):

$$\Gamma_{2p}^{1e} = \left[\frac{E_Z^2\Delta^2}{(\Delta^2 - E_Z^2)^2}\right] \frac{m_t^2(\beta_D - \alpha_R)^2 E_{v'v}^5}{4\pi\rho\hbar^8}(TA + LA)\, \left[y_{0m_1}^4 + x_{0m_1}^4\right]; \tag{S14}$$

here $(TA+LA) \equiv \int_{-1}^{1} dx\, \Xi^{(\sigma)}(x)(1-x^2)/v_\sigma^7$ accounts for contribution of transverse and longitudinal acoustic phonons. Numerical fit to the 1-electron experimental data for $E_{\rm VS} = 2.8\,T$ shows that this relaxation mechanism has to be taken in to account in order to describe the data above anticrossing. The fit is consistent with $1s-2p$ dipole matrix elements about twice bigger than for a parabolic QD, of the order of $\approx 10\,$nm.

2-electron case ΔE^7 corrections

An analogous calculation in the 2-electron case was performed as well. We examined virtual excitations to the whole set of excited states that includes the triplet valley states, the upper singlet valley state, and the singlet and triplet states, involving orbital single-electron states. We found that the only relevant state (capable to produce a relaxation rate correction of ΔE^7 behavior) is the valley-spin-orbital state: $|m_1'', T\rangle = \frac{1}{\sqrt{2}}\left[\varphi_2(\boldsymbol{r}_1)\varphi_{m1}(\boldsymbol{r}_2) - \varphi_2(\boldsymbol{r}_2)\varphi_{m1}(\boldsymbol{r}_1)\right] \otimes |T_-\rangle$, where one of the electrons is occupying $|v_2\rangle$ state, while the other is orbitally excited. We have derived a contribution to the relaxation rate, $\Gamma_{2p}^{2e} \propto\sim E^7$, similar to the 1-electron case. However, including this contribution does not help to fit better the 2-electron data for reasonable parameters.

Best fit parameters

For the best fit to the 1-electron and 2-electron experimental data we use:
(1) SOC strength $\beta_D - \alpha_R \approx 45 - 60\,$m/s, which is justified, since the electric field in the experiment is $\approx 3\times 10^7\,$V/m.
(2) We take (for each $E_{\rm VS}$) that $|\boldsymbol{r}_{12}| \simeq |\Delta\boldsymbol{r}_{12}| \equiv |\boldsymbol{r}_{11} - \boldsymbol{r}_{22}|$ (justified by common sense and preliminary calculations).
(3) Splitting to the first orbital excited state, $\Delta = 8\,$meV (1-electron case) and $\Delta_2 = 4\,$meV (2-electron case) taken from experimental values.
(4) In the 1-electron fit, the $1s-2p$ dipole matrix elements are $x_{0m_2} = y_{0m_1} \simeq 1.8\sqrt{\frac{\hbar^2}{2m_t\Delta}}$ (a plausible assumption for a non-parabolic dot), and in the 2-electron case we take the same values for these matrix elements. Least-square fit to the data then reveals the valley dipole matrix elements for each set of data, as follows: $r_{28} = 1.1\,$nm ($E_{\rm VS} = 0.33\,$meV), $r_{65} = 1.7\,$nm ($E_{\rm VS} = 0.75\,$meV) in the 1-electron case, and $r_5^{2e} = 4.8\,$nm ($E_{\rm VS} = 0.58\,$meV) in the 2-electron case, consistent with our expectations.

Supplementary Note 4

The TCAD model of the real device geometry is shown in Supplementary Figure S2 (a). As mentioned in the main article, in our simulations we use the same voltage range as in the experiments and the only free parameter is the Si/SiO_2 interface charge, $Q_{\rm ox}$. This has been chosen to match the experimental threshold voltage ($V_{\rm th}$=0.625 V). In Supplementary Figure S2 (b) the dependence of $V_{\rm th}$ on $Q_{\rm ox}$ is reported. This has been evaluated by integrating the charge density in a region of the 2DEG near the interface as all the gate voltages are simultaneously swept (see inset). The value of choice is $Q_{\rm ox} = -4.5\times 10^{11}\ {\rm cm}^{-2}$. The vertical electric field profile in the (x,z) plane at $V_{\rm P}$=1.4V is shown in Supplementary Figure S2 (c). As highlighted in the main article, the QD is formed in the region where the conduction band falls below the Fermi energy, so that the vertical interface field therein is the one relevant to calculate the valley splitting. Finally, with the same methodology illustrated in the paper, the dependence of the valley splitting (at $V_P = 1.4$V) on the interface charge density has been estimated with both the atomistic and the effective mass theories, and is shown in Supplementary Figure S2 (d). It is of note that the variation of $E_{\rm VS}$ with interface charges is relatively small and cannot account for the large offset between computed and experimental values. Hence, we believe that the main factors that reduce valley splitting in this nanostructure are due to interface effects (as discussed in the main article).

Supplementary References

[52]Yu, P. & Cardona, M. *Fundamentals of Semiconductors* (Springer, Berlin, 2010).